Unraveling the dual defect effects in C_3N_5 for piezo-photocatalytic degradation and H_2O_2 generation

Cheng Fu, Mengyu Zhao, Xuan Chen, Guowei Sun, Chan Wang, Qijun Song [*]

Key Laboratory of Synthetic and Biological Colloids, Ministry of Education, School of Chemical and Material Engineering, Jiangnan University, 1800 Lihu Road, Wuxi, Jiangsu Province 214122, PR China

ABSTRACT

An efficient piezo-photocatalyst (C_3N_{5-x}-CN) with enhanced piezo-photocatalytic performance was successfully fabricated by introducing cyano groups (-CN) and N vacancies into the semiconductor C_3N_5 through a two-step thermal polymerization/etching procedure. As-prepared C_3N_{5-x}-CN exhibits a synergistic enhancement of piezoelectricity and photoelectricity in ultrasound-assisted photocatalytic system. Experimental characterization and computer simulations confirmed that the introduction of dual-defect sites in C_3N_5 creates an active catalytic surface, which not only increases the piezoelectricity, but also promotes the carrier separation, thus achieving an overall improved piezo-photocatalytic performance. The piezo-photocatalytic system enables efficient removal of tetracycline with a kinetic constant of 0.0342 min^{-1} and this figure is increased to 0.0492 min^{-1} in the presence of PMS. Furthermore, a yield of 1359 µmol/g/h of H_2O_2 was produced under piezo-photocatalytic treatment of pure water. The synergistic mechanism and relative activity of dual-defect sites unraveled in this work could facilitate the construction of a multifunctional platform for carbon-nitride based piezo-photocatalysis.

1. Introduction

Photocatalysis is currently a focus for environmental remediation and generation of value-added chemicals via direct conversion of solar energy [1–6]. However, its efficiency is still far from satisfactory due to the rapid carrier recombination in catalyst [7]. The piezo-phototronic effect is believed to be one of the effective techniques to prevent or alleviate the carrier recombination [7,8]. The internal electric field generated via mechanical stimulation could induce polarization, which facilitates photo-generated carrier separation and promotes the subsequent catalytic process. Since the proposal of piezo-phototronics, metal-based materials represented by ZnO, BaTiO$_3$, BiFeO$_3$, MoS$_2$ have been successively developed, and they have achieved excellent catalytic efficiency in pollutant removal, disinfection, and H_2O_2 generation [9–15]. However, metal-based piezo-photocatalysts inevitably have the risk of metal leaching, thus limiting their practical applications. Hence the development of carbon-based piezo-photocatalyst has theoretical and practical significance for environmental remediation or producing value-added chemicals.

Nitrogen-rich carbon nitrides are a class of emerging nonmetallic semiconductors [16–22]. As an excellent representative, C_3N_5 has

exhibited better electrocatalytical and photocatalytical performance than the conventional C_3N_4 [16–19]. Our earlier work also demonstrated that C_3N_5 has remarkable piezocatalytic activity, which can be further enhanced by defect engineering [23]. It is expected that the effective separation of photo-generated carriers could be achieved with the assistance of piezoelectric field, endowing C_3N_5 with high piezo-photocatalytic activity. Additionally, defect engineering could further optimized the electrical structure of C_3N_4 or C_3N_5, leading to an enhanced light absorption, carrier separation efficiency and photocatalytic activity [5,24–26]. Since defect engineering is beneficial for both piezocatalysis and photocatalysis, it is foreseeable that defect engineering could also enhance the piezo-photocatalytic performance of C_3N_5. In this aspect, many previous works have focused on the magnitude of the piezoelectric potential of catalysts [27], while the involvement of the carriers in the chemical reaction was largely ignored. The engagement of these carriers in chemical processes could be better understood by investigating on the adsorption, electron transfer, and active species produced on the catalyst surface [27]. Defect engineering can also improve the photocatalytic performance by optimizing the electronic structure of catalyst [28]. For example, defect-induced electronic structure optimization can alter the adsorption and activation behaviors

of key species [29]. Compared to the pristine BaTiO$_3$, the O vacancies containing BaTiO$_3$ has a reduced piezoelectric response and enhanced piezocatalytic performance, which is attributed to the optimization of the electronic structure and enhancement of O$_2$ adsorption/activation [30]. The –CN substitution and N vacancies constructed in C$_3$N$_4$ show synergistic effect and enhance the photocatalytic efficiency by optimizing the band structure [5]. Therefore, it is necessary to investigate the relative activity and synergistic effect of different defect sites, which could provide further insights into the development of high-performance nitrogen-rich carbon nitride piezo-photocatalysts.

In this work, C$_3$N$_5$ was selected as a model carbon nitride for the subsequent exploration. The piezo-photocatalyst with -CN substitution and N vacancy was synthetized via a two-step thermal polymerization and thermal etching strategy. A multifunctional piezo-photocatalytic platform was constructed to achieve piezo-photocatalytic degradation, H$_2$O$_2$ production, and peroxymonosulfate (PMS) activation. As expected, a high piezo-photocatalytic efficiency is achieved thanks to the defect engineering optimized electronic structure, the enhanced light absorption of the catalyst and the improved adsorption of relevant substrates.

2. Experiment

All the chemicals, characterization methods, computational framework, and experimental methods are detailed in 'Supporting Information'. Tetracycline, ciprofloxacin, methylene blue, and rhodamine b, respectively abbreviated as TC, CIP, MB, and RhB are used as the model pollutants. The synthesis of control samples are also described in 'Supporting Information' and their symbols are summarized as follows: C$_3$N$_5$ (pristine C$_3$N$_5$), C$_3$N$_5$-CN (C$_3$N$_5$ with -CN), C$_3$N$_4$ (pristine C$_3$N$_4$).

2.1. Synthesis of dual-defect C$_3$N$_5$ (C$_3$N$_{5−x}$-CN)

As shown in Fig. 1a, a typical process for the synthesis of C$_3$N$_5$-CN is the carbonization of a mixture of 0.8 g 3-amino-1,2,4-triazole and 0.2 g thiourea at 500 °C for 3 h at a ramp rate of 5 °C/min. To get the C$_3$N$_{5−x}$-CN, 0.5 g of C$_3$N$_5$-CN was re-pyrolyzed at 500 °C for 3 h.
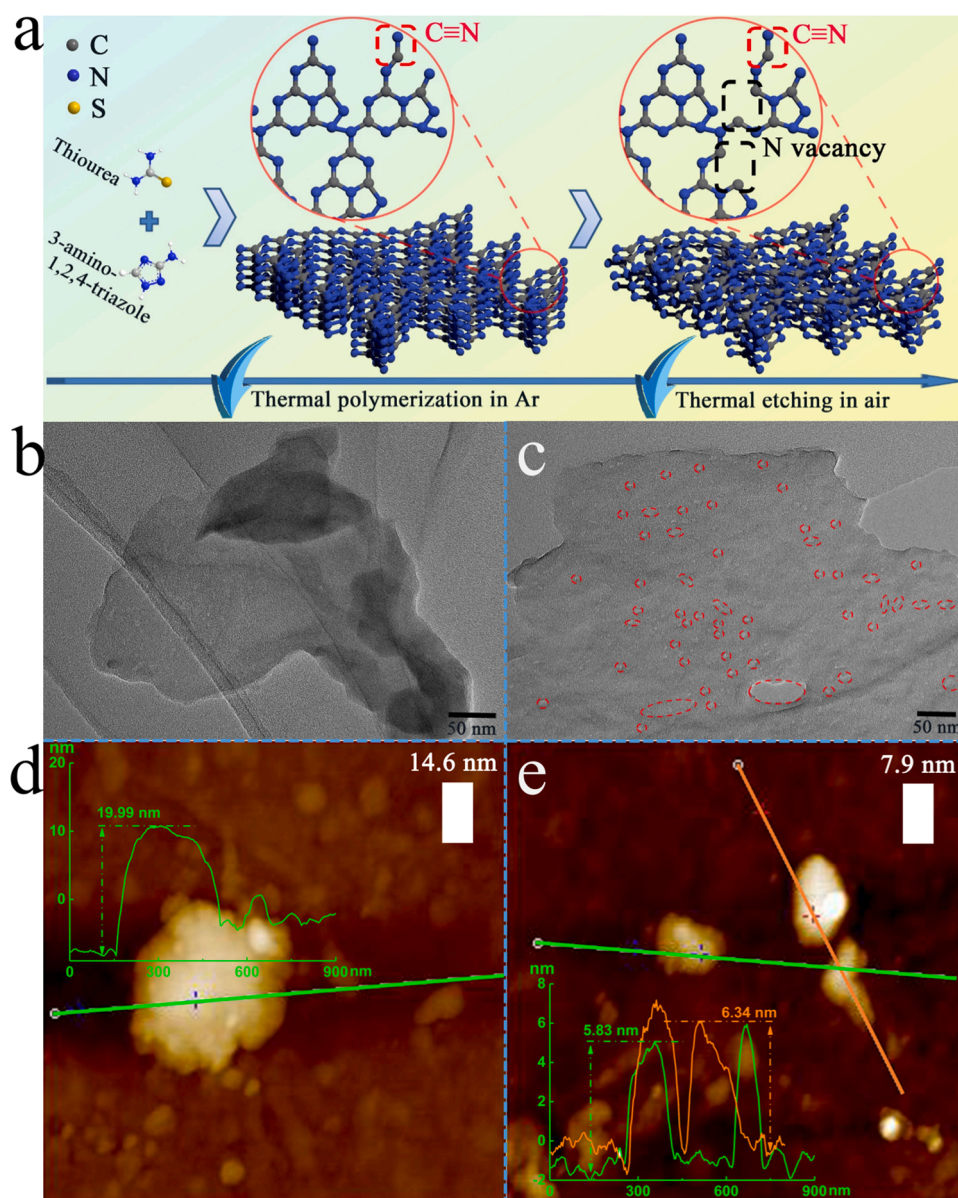
Fig. 1. (a) The synthetic route of C$_3$N$_{5−x}$-CN. TEM image of (b) C$_3$N$_5$-CN and (c) C$_3$N$_{5−x}$-CN. AFM image and corresponding height curves (inset) of (d) C$_3$N$_5$-CN and (e) C$_3$N$_{5−x}$-CN.

3. Results and discussion

3.1. Synthesis and characterization of C_3N_5-based catalysts

C_3N_5 is an emerging semiconductor with high electrocatalytic, photocatalytic, and piezocatalytic performance [16–19,23]. Here, we systematically investigated the principle of piezoelectrically assisted photocatalytic performance enhancement of dual-defect C_3N_5. To better understand the synergistic effect, key mechanism, and relative activity of the two defect sites, we first characterized the $C_3N_{5−x}$-CN in details as which possesses the best catalytic performance.

TEM and AFM data (Fig. 1b-e) confirm that $C_3N_{5−x}$-CN is more porous and thinner than C_3N_5-CN, which facilitates the exposure of active sites and is more conducive to polarization enhancement. Similarly, the thin layer of C_3N_4 achieves stronger in-plane polarization and improved catalytic efficiency [31]. The SEM images (Fig. S1 a-d) show that all materials exhibit relatively similar morphologies, indicating that the defect engineering does not unduly damage the primary structure of C_3N_5. The photographs of different carbon-nitride catalysts are summarized in Fig. S1 e. The $C_3N_{5−x}$-CN was further characterized by EDS mapping (Fig. S2), and a uniform distribution of C/N elements could be observed. Piezoresponse force microscopy (PFM) was employed to measure the piezoelectricity of $C_3N_{5−x}$-CN , it can be seen from the amplitude image (Fig. S3a) and phase image (Fig. S3b) that the difference of the amplitude and phase in different regions implies the distinguished polarization direction and polarization degree [32].

Moreover, a clear butterfly amplitude loop and a local hysteresis loop are observed in Fig. S3c, proving that $C_3N_{5−x}$-CN possesses a piezoelectric response. Compared to our previous data [23], $C_3N_{5−x}$-CN has a stronger piezoelectric response than the pristine C_3N_5.

The crystal structures of all the catalysts were analyzed via X-ray diffraction (XRD). The characteristic peaks of all catalysts are distributed between 13.1° and 13.4° and 27.2–27.7°, corresponding to the typical (100) and (002) planes of the carbon nitrides [17,19,31,32]. The (100) plane intensity of $C_3N_{5−x}$-CN is relatively weaker than that of the pristine C_3N_5 and C_3N_5-CN, implying that the introduction of -CN and N vacancies leads to the formation of in-plane defects. The intensity of the (002) plane of $C_3N_{5−x}$-CN also decreases, suggesting a weakening of the interlayer stacking effect and the formation of a thinner layer structure. These results are supported by the AFM observations, which also consistent with that observed in the traditional C_3N_4 [5,31]. To understand the defect formation process more deeply, formation energy calculations were performed for different C_3N_5-based catalysts. As shown in Fig. S4 and Table S1, the N vacancy is most likely to be formed at the N position 10 in the triazine structure, which should be responsible for the further decrease in the intensity of the (100) peak of $C_3N_{5−x}$-CN.

The Fourier-transform infrared (FTIR) spectra were used to compare the functional groups in C_3N_5-based materials and C_3N_4 (Fig. 2b). The introduction of -CN was confirmed by the appearance of the characteristic peak at 2175 cm^{-1} for –CN [5]. The characteristic peaks at 810 and 891 cm^{-1} are higher in C_3N_4 than C_3N_5, suggesting less C-N bonds in C_3N_5 [16]. The characteristic peaks of the triazine moiety were further
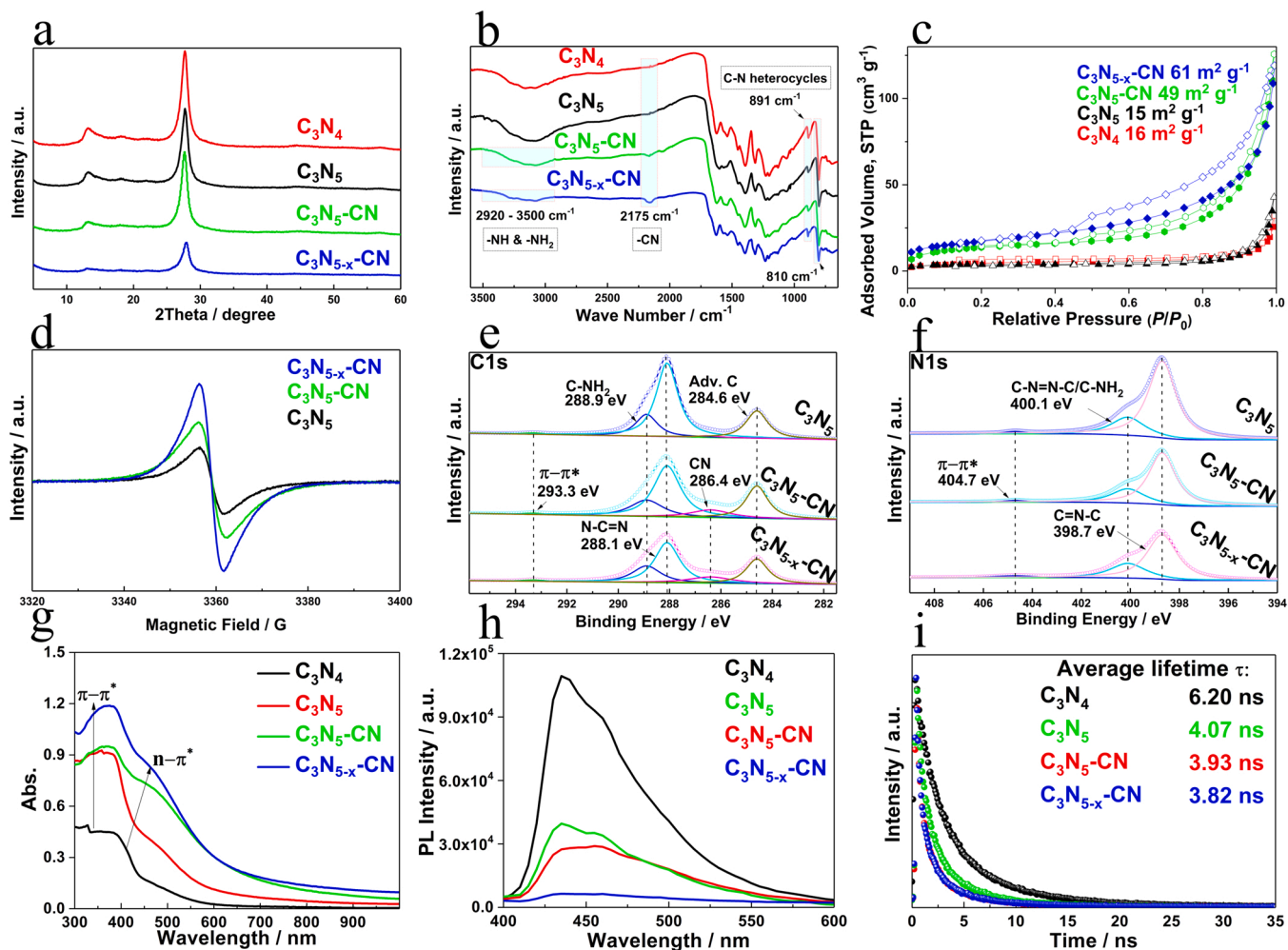

Fig. 2. (a) XRD patterns, (b) FTIR spectra, (c) BET data, (d) EPR data, (e) C 1 s XPS, (f) N 1 s XPS, (g) UV–vis DRS, (h) PL spectra, and (i) TRPL data of different catalysts.

lowered in the defect C_3N_5 than in pristine C_3N_5, indicating that the defects are produced after the partial elimination of triazine moiety, which is also consistent with the data of formation energy. In carbon nitrides, the wide peaks in 2920–3500 cm^{-1} was attributed to N-H stretching vibrations [5]. These characteristic peaks in C_3N_{5-x}-CN are significantly weaker compared to that in C_3N_5-CN due to the breakage of the N-H bond after re-carbonization. The breakage of the interlayer N-H bond leads to the formation of a thin layer structure, which is also consistent with the XRD data. In addition, the BET data indicate an increase in the specific surface area for the re-carbonized material (Fig. 2c, 61 m^2/g), which could be attributed to the formation of thin-layer structures and the defects induced exposure of surfaces.

Electron paramagnetic resonance (EPR) was employed to establish the relationship between unpaired electrons and defect states since defect engineering might change the electronic structure of materials [33,34]. As can be observed in Fig. 2d, the Lorentzian signals of C_3N_{5-x}-CN and C_3N_5-CN are larger (g-factor, 2.003) than that of pristine C_3N_5, because the electron-withdrawing nature of -CN could concentrate and delocalize the isolated valence electrons in the π-conjugated heterocyclic rings [5,33,35–37]. Compared to C_3N_5-CN, the Lorentzian signal of C_3N_{5-x}-CN is further increased, demonstrating that N vacancy promotes the formation of unpaired electrons. In previous works, it was also confirmed that concentration of delocalized electrons can promote the photocatalytic performance [36,37]. Similarly, the dual-defect C_3N_5, an electron-rich structure, may facilitate the provision of more electrons to participate into the piezo-photocatalysis. And the experiment facts also prove that C_3N_{5-x}-CN possesses high piezo-photocatalytic efficiency.

Fig. 2e, f and Table S2 illustrate the X-ray photoelectron spectroscopy (XPS) data of all C_3N_5-based materials, which are used to further reveal the defect states. In the high-resolution C 1 s spectra, the characteristic peaks at 288.9, 288.1, and 284.6 eV belong to C-NH$_2$, N = C-N, and adventitious C (Adv. C), respectively [19]. Clearly, the additional characteristic peaks in C_3N_{5-x}-CN and C_3N_5-CN located at 286.4 eV belong to –CN group, indicating the successful introduction of –CN [5]. Additionally, the delocalization of π electron is responsible for the two weak peaks at 293.3 eV (C 1 s spectra) and 404.7 eV (N 1 s spectra), showing graphitic stacking in C_3N_5, C_3N_5-CN, and C_3N_{5-x}-CN [17,35]. The peaks in the high-resolution N 1 s spectra at 398.7 eV and 400.1 eV can be ascribed to the C=N-C and bridging nitrogen atoms (C-N = N-C) or C-NH$_2$, demonstrating the presence of both triazine and triazole moiety in all structures [17,19,38]. The proportions of several N species are summarized in Table S2. The peak intensities of C=N-C in C_3N_{5-x}-CN and C_3N_5-CN are much lower than that in the pristine C_3N_5, indicating that defect engineering partially destroyed the triazine structures. The result is consistent with that observed from the formation energy (Table S1) and FTIR data (Fig. 2b). Elemental analyses were performed to more accurately determine the composition of the different catalysts. The atomic ratios of C/N and C/H for the different catalysts are summarized in Table S3. C_3N_5 exhibits a lower C/N ratio than that of C_3N_4, the relatively increased N content could be attributed to the retention of some triazole moieties in C_3N_5. Among the C_3N_5-based materials, C_3N_{5-x}-CN possesses the highest C/N and C/H values, which is consistent with the formation energy and FTIR results, indicating that defect engineering leads to increased loss of N and H atoms.

To further understand the effect of defect engineering on the photoelectrical attribution of C_3N_5, the UV–vis diffuse reflectance spectra (DRS), the steady-state photoluminescence (PL) emission spectra, and the time-resolved photoluminescence (TRPL) of all the samples were measured and the results are summarized in Fig. 2g-i. As seen in Fig. 2g, the absorption band produced by the π→π * electronic transition of C_3N_{5-x}-CN was noticeably enlarged in comparison with that of the pristine C_3N_5, and additional absorption bands developed as a result of the n→π * electronic transition of the lone pair of electrons at -CN and N vacancies [39–41]. The new absorption bands signify the improvement

in light absorption and the optimized electronic structure by the defect engineering. Fig. S5 lists the data of band gaps, where the Eg value of C_3N_5 is reduced from 1.98 eV to 1.68 eV after defect engineering. And the positions of the valence and conduction bands were further determined from the Mott Schottky data (Fig. S6). Fig. 2h shows that the defect engineering leads to a decrease in luminescence intensity of C_3N_5, indicating that the dual-defects exhibit a synergistic effect to efficiently promote carrier separation. The TRPL spectra in Fig. 2i shows the changes of carrier dynamics after the defect engineering. The fitted results (Table S4) show that the average radiation lifetimes of C_3N_4, C_3N_5, C_3N_5-CN and C_3N_{5-x}-CN are 6.20, 4.07, 3.93 and 3.82 ns, respectively. The decay of lifetime should be attributed to the fact that the dual-defect sites could capture electrons efficiently and thus inhibit carrier recombination [5].

Using Kelvin probe force microscopy (KPFM) and electrochemical investigations, the surface potential and electron transport properties of C_3N_{5-x}-CN are examined to clarify the piezoelectrically strengthened photocatalysis. The KPFM measurements were conducted under light or dark condition (Fig. 3a, b). The results confirm that the voltage difference is 20.3 mV in dark and drops to 15.2 mV under light, suggesting that the charge response of C_3N_{5-x}-CN was attenuated under illumination conditions. A similar phenomenon was observed in conventional carbon nitride [31]. However, the decrease in piezoelectric potential may lead to a decrease in piezo-photocatalytic activity, contrary to the current experimental results of piezoelectric enhanced photocatalysis. Driven by ultrasound-induced alternating mechanical vibrations, the direction of the piezoelectrically excited electric field is reversed repeatedly, resulting in rapid recombination of the piezocarriers. The enhancement in the charge transfer between the substrate and the catalyst could allow more surface charges to participate in chemical reactions and achieve higher catalytic performance. Although the light-induced carriers are partially depleted by compensating the polarization charge, the residual piezoelectric charges can rapidly participate in the redox reactions on the surface of C_3N_{5-x}-CN in piezo-photocatalytic system. The transient current response experiments and electrochemical impedance spectroscopy (EIS) tests demonstrate that the enhanced charge transfer plays the key role in the improvement of the piezo-photocatalytic performance. Fig. 3d illustrates that the catalytic system produces a higher current response after defect engineering, which should be accountable for the high catalytic performance of C_3N_{5-x}-CN. Fig. 3e shows that the photoelectric response is significantly enhanced with the assistance of ultrasound, indicating the synergistic effect of piezoelectricity and photoelectricity. A similar phenomenon was observed in the piezo-photoactivated PMS system (Fig. 3g, h), demonstrating that the piezo-photocatalytic system can promote the activation of PMS by enhancing charge transfer. The EIS data (Fig. 3f, i) also confirm that defect engineering reduces the impedance of the piezo-photocatalytic system and a synergic effect of piezoelectricity and photoelectricity was observed. The simulation results in Fig. 4 show that the energy gap of C_3N_5 is narrowed by the defect engineering, which is consistent with the experiment data. The small energy gap effectively facilitates the potential-driven electron transfer. The introduction of -CN and N vacancies can also increase the dipole moment of catalyst (Fig. S7), confirming that defect engineering raises the polarization of C_3N_5.

By summarizing the above characterizations, electrochemical data and computer simulations, we can conclude that defect engineering not only increases the polarization to improve the piezoelectric response but also optimizes the electronic structure to accelerate carrier separation. Thus, significantly improved piezo-photocatalytic performance was achieved by using C_3N_{5-x}-CN as the catalyst.

3.2. Piezo-photocatalytic performance

3.2.1. Piezo-photocatalytic degradation

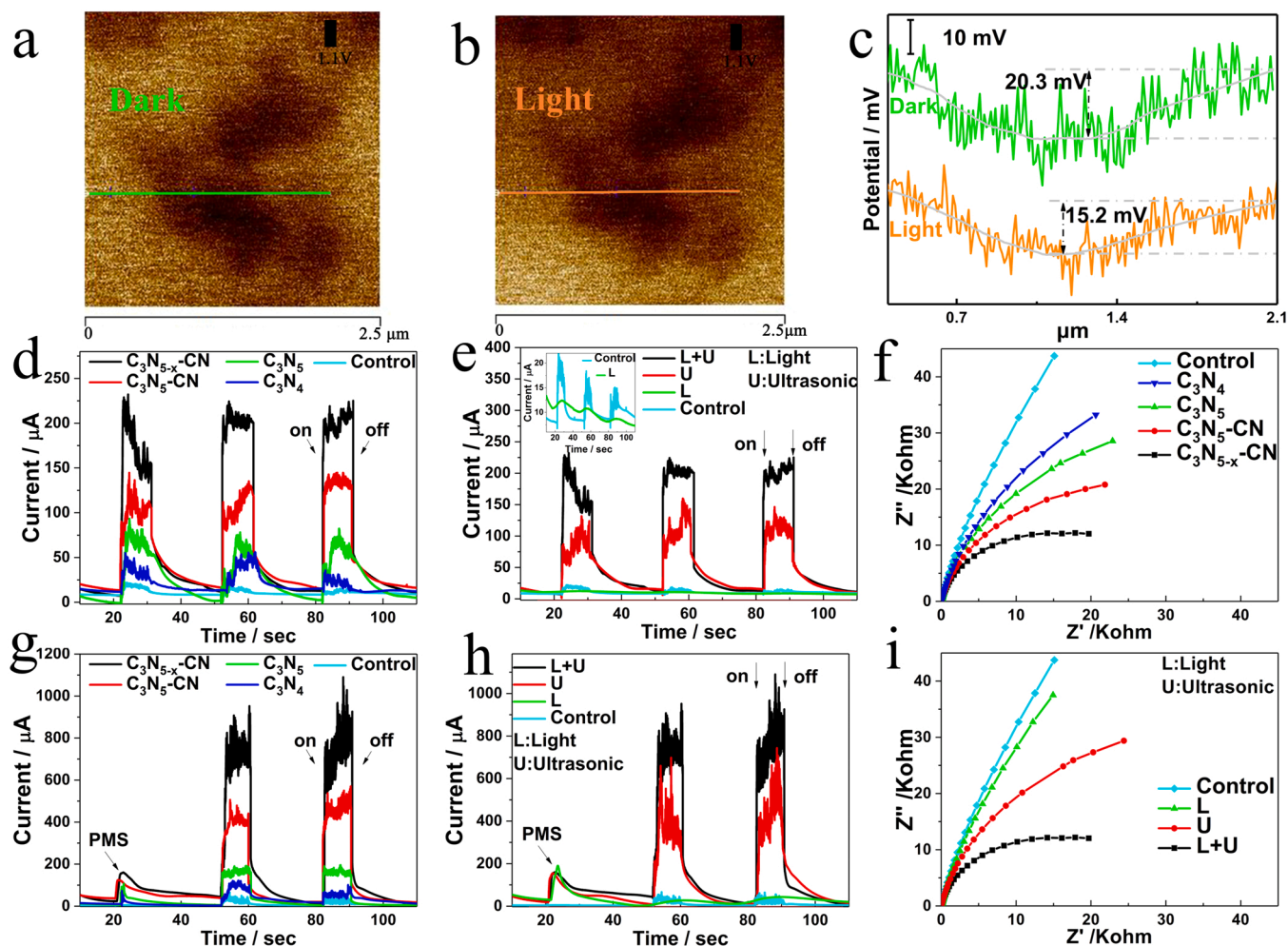To evaluate different piezo-photocatalytic systems, we initially

Fig. 3. KPFM potential data of C_3N_{5-x}-CN in the dark (a), under illumination (b), and the corresponding surface potential curves (c). Transient current response of different system: in the absence of the PMS (d, e), in the presence of the PMS (g, h). EIS data of different system (f, i).
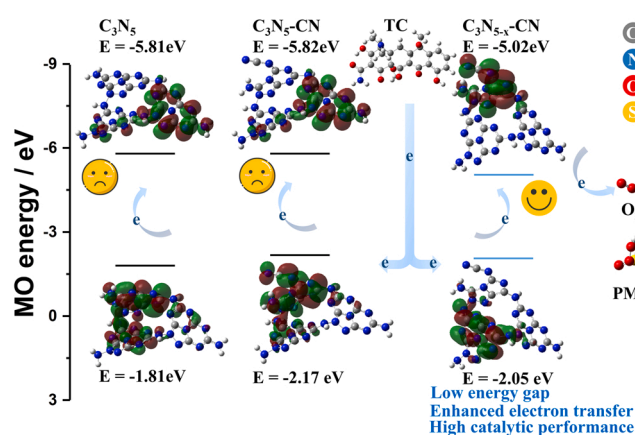

Fig. 4. Schematic diagram of electron transfer driven by potential energy difference.

examined the performance of different catalysts using the simulated dye wastewater (RhB, 20 ppm). As shown in Fig. 5a and Fig. S8, when C_3N_{5-x}-CN was used as the catalyst, the removal of pollutant can be achieved in 30 min, with a kinetic constant of 0.1218 min^{-1}, which is substantially higher than that obtained from pristine C_3N_5 and CN-modified C_3N_5. And the kinetic constant is 3–4 times greater than that obtained from the piezocatalysis or photocatalysis along. These results

clearly demonstrate the high synergistic effect of the dual defects in C_3N_{5-x}-CN. The catalytic performance of C_3N_{5-x}-CN was also substantially better than that obtained from the commercially available piezo-photocatalyst BaTiO$_3$ and ZnO (Fig. S9), suggesting that the C_3N_{5-x}-CN has a great potential for practical application. The applicability of our piezo-photocatalytic system was verified for different pollutant CIP, TC, and MB with the kinetic constants of 0.0161, 0.0342, and 0.0401 min^{-1} respectively (Fig. 5b and Fig. S10). As shown in Fig. S11, only about 5% of the antibiotic or 25% of the dye can be degraded in the absence of C_3N_{5-x}-CN, indicating the critical role of the catalyst in the piezo-photocatalytic system. Fig. 5c shows that the removal of TC can be achieved over a wide range of pH (3−11) and the degradation rate of TC was increased slightly under alkaline conditions. This could be due to TC has reduced stability in alkaline condition [42,43] and the deprotonation of H$_2$O$_2$ in alkaline condition accelerates the formation of ROS [44].

The effects of catalyst dosage, ultrasonic power, pollutant dosage, and temperature on the piezoelectric photocatalytic system were further explored (Fig. 5d). When the dose of catalyst was increased from 100 mg/L to 500 mg/L, the removal rate of TC increased from 58% to 89% in 60 min. When the ultrasonic power was reduced to 40% of the initial power, the removal rate of TC decreased to about 77%. The effect of pollutant concentration was also investigated, a very high removal rate of 99% can be obtained for 10 ppm TC in 60 min, while this figure decreased to about 60% for 50 ppm TC. Although TC decomposition is an endothermic reaction, increasing the temperature is not conducive to the piezo-photocatalytic removal of TC, which should be attributed to
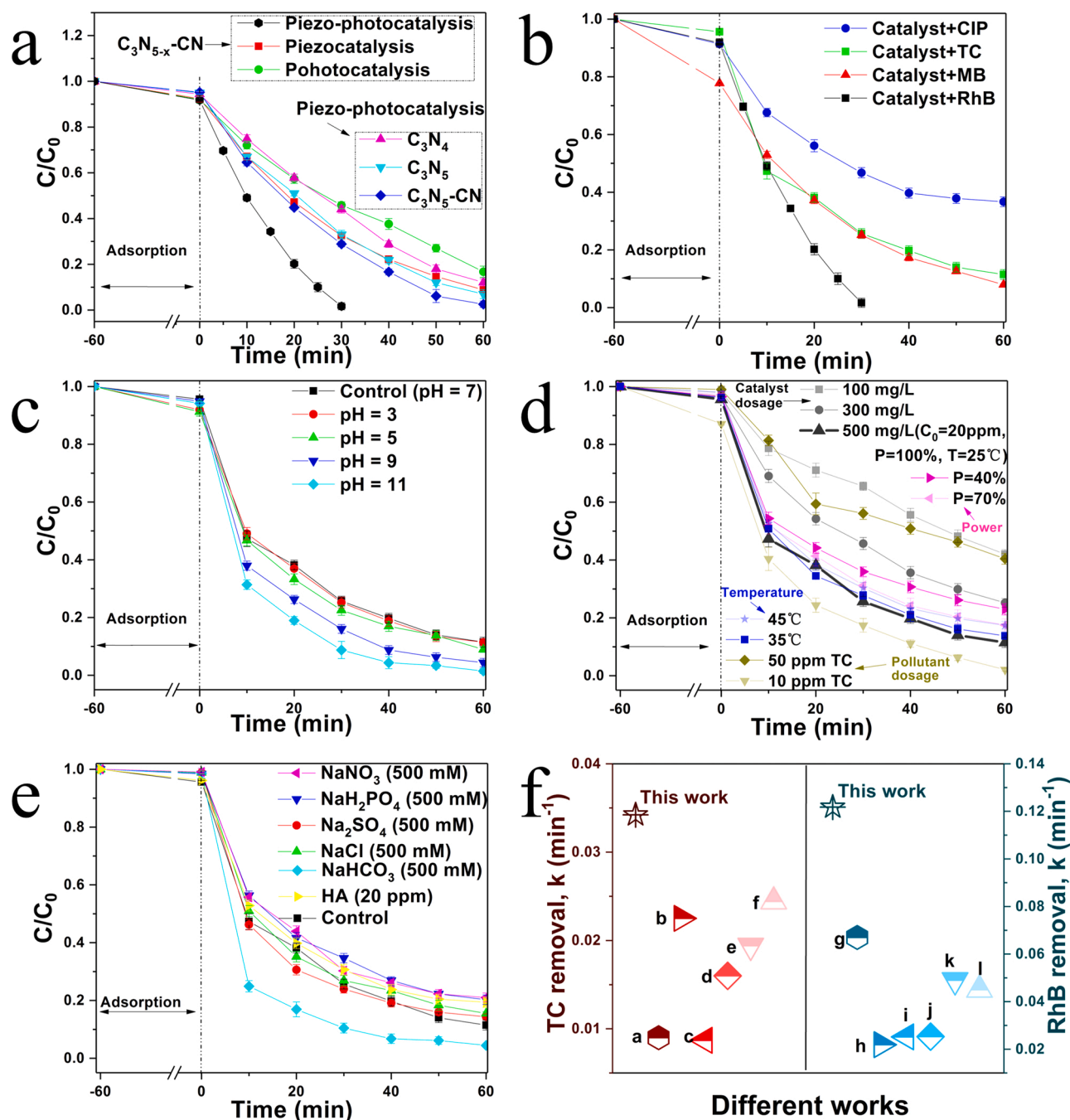
Fig. 5. (a) Piezo-photocatalytic degradation performances of different catalysts for degradation of 20 ppm RhB. (b) Degradation performance of different refractory pollutants. Effect of (c) different pH, (d) catalyst/pollutant dosage, power, temperature, (e) background anion, and natural organic matter on the degradation of TC (20 ppm) by C_3N_{5-x}-CN piezo-photocatalytic system. (f) Kinetic constants for TC or RhB degradation of similar catalytic systems.

the fact that the high temperature reduces the dissolved oxygen content and thus affects the production of ROS and the subsequent removal of pollutants [45,46]. Considering the possible presence of natural organic pollutants and background anions in the real wastewater, we continued to explore the effects of humic acid and several anions on the piezo-photocatalytic system (Fig. 5e and Fig. S13). As in Fig. S13, low concentration of humic acid or background anions have little effect on the piezo-photocatalytic system. But high concentrations of NO_3^- and $H_2PO_4^-$ (500 ppm) exhibited an inhibition effect on the removal of TC, which could be attributed to their quenching effect on ·OH and their competitive adsorption on surface of catalyst [47,48]. It is interesting to note that HCO_3^- has demonstrated a beneficial impact on the degradation of TC, which could be related to its activating effect on H_2O_2 in ROS

formation [49]. Compared with other recently reported piezocatalysts/piezo-photocatalysts, the C_3N_{5-x}-CN system exhibited a competitive removal rate for TC or RhB [30,50–60] (Fig. 5f).

To better understand the degradation mechanism, the intermediate products of TC were analyzed by HPLC-MS. As shown in Fig. S14, six degradation intermediates with mass peaks at 461 (P1), 475 (P2), 427 (P3), 274 (P4), 338 (P5), and 274 (P6) were found in the C_3N_{5-x}-CN piezo-photyocatalytic system [61–63]. Based on these results, the possible degradation pathways are presented in Fig. S14d, where the main routes involve terminal oxidation, dealkylation, deamination and ring opening. The ring-opening products may then be transformed into CO_2, H_2O, and other low molecular products in the subsequent degradation steps.

3.2.2. Piezo-photocatalytic H₂O₂ evolution and PMS activation

The C₃N₅₋ₓ-CN piezo-photocatalytic system was evaluated for H₂O₂ generation and PMS activation. Fig. S15 shows the standard curve for the dependence of absorbance on the H₂O₂ concentrations. Similar to the piezo-photocatalytic degradation data, C₃N₅₋ₓ-CN exhibited the highest catalytic performance, as a yield of 1359 μmol/g/h H₂O₂ was readily achieved in the absence of any sacrificial agents (Fig. 6a). This yield is more than 1.9 times of that obtained from pristine C₃N₅ and is also significantly greater than that obtainable from the commercial BaTiO₃ and ZnO. In contrast, the H₂O₂ yield was almost negligible in the absence of catalyst, indicating the critical role of C₃N₅₋ₓ-CN. To further explore the ultrasound assisted photocatalytic enhancement phenomenon, the H₂O₂ yields of the piezoelectric and photocatalytic systems were evaluated separately (Fig. 6b). The H₂O₂ yield of the piezo-photocatalytic system was 2.2 times higher than that of the piezoelectric system and 9.2 times higher than that of the photocatalytic system, which clearly demonstrates the piezoelectric and photoelectrical synergistic effects of C₃N₅₋ₓ-CN. In comparison with other recently developed photocatalytic, piezocatalytic, and piezo-photocatalytic systems for H₂O₂ generation [4,32,45,46,64–68], the metal-free C₃N₅₋ₓ-CN exhibits a competitive catalytic performance (Fig. 6d). Combined with the electrochemical data (Fig. 3), the high H₂O₂ yield should be attributed to ultrasound assisted carrier transfer, leading to the rapid participation in the redox reactions.

Quenching experiments were used to further explore the mechanism of H₂O₂ generation in the C₃N₅₋ₓ-CN piezo-photocatalytic system (Fig. 6c). As a quencher for·OH [66], isopropanol (IPA) exhibited an acceleration effect, showing that·OH is not the key species for H₂O₂ generation and IPA can act as a sacrificial agent to promote the production of H₂O₂. In contrast, p-benzoquinone (BQ), as a quencher of O_2^-, showed a highly inhibitory effect on H₂O₂ production, indicating that the generation of O_2^- is the primary step for H₂O₂ evolution [5,32,69,70]. Similarly, ¹O₂ quencher furfuryl alcohol (FFA) [32] exhibited an inhibition effect, indicating that the production of ¹O₂ is also a key step in the H₂O₂ generation process. In the absence of O₂ (Fig. S16), the production of H₂O₂ is almost totally suppressed, showing that O₂ reduction is the essential step for H₂O₂ production. The hole (h^+) quencher ethylenediaminetetraacetic acid disodium salt (EDTA-2Na) exhibited a little inhibition on H₂O₂ production [32], suggesting that h^+ is not the major species for the formation of H₂O₂. Based on these quenching experiments, it can be concluded that C₃N₅₋ₓ-CN piezo-photocatalytic production of H₂O₂ depends mainly on O₂ reduction (Eq. 1) rather than water oxidation (Eq. 2).

$$O_2 + 2e^- + 2H^+ \rightarrow H_2O_2 \tag{1}$$

$$2H_2O + 2h^+ \rightarrow H_2O_2 + 2H^+ \tag{2}$$
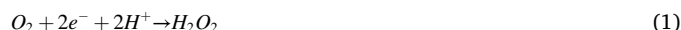
PMS activation is a promising advanced oxidation processes (AOPs)
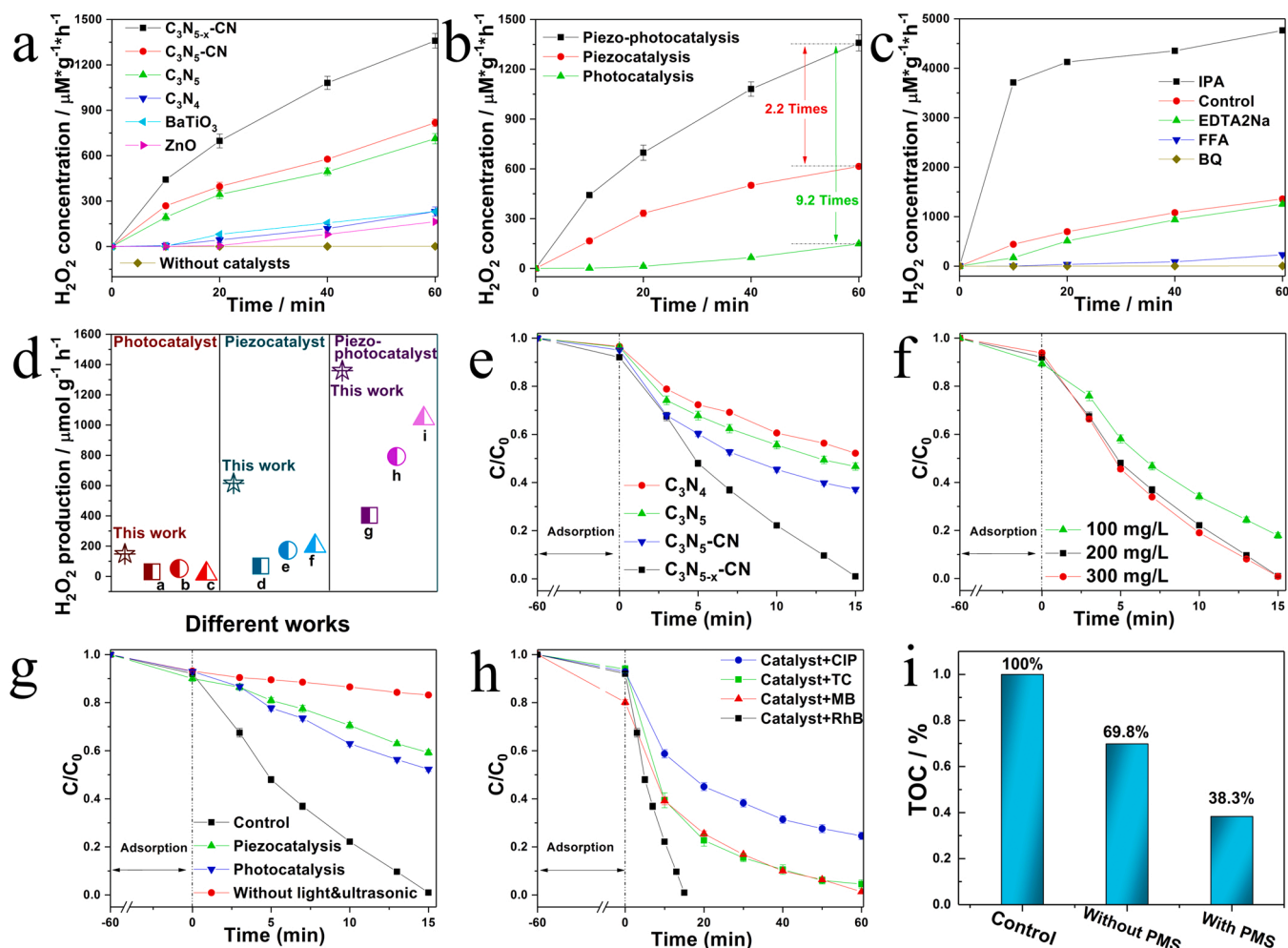
Fig. 6. (a) Piezo-photocatalytic H₂O₂ evolution of different catalysts, (b) H₂O₂ evolution of different system. (c) Quenching experiments of H₂O₂ evolution system. (d) H₂O₂ yield in a similar catalytic system. (e) The performance of piezo-photocatalytic activation of PMS to removal RhB (20 ppm). (f) The effect of PMS dosage in piezo-photocatalytic activation of PMS. (g) Performance comparison of different PMS activation system. (h) Degradation performance of different refractory pollutants. (i) TOC data.

for the removal of organic pollutants [71]. Photocatalysis and piezocatalysis are environmentally friendly ways to activate PMS [72–74], but their activation efficiency is not very satisfactory due to the carrier recombination. Considering that the piezo-photocatalytic system can achieve more efficient carrier separation [7,8], we performed PMS activation with the C_3N_{5-x}-CN piezo-photocatalytic system. The results are presented in Fig. 6e and Fig. S17, where it can be seen that C_3N_{5-x}-CN can achieve more efficient removal of contaminant when compared with the data obtained from commercial $BaTiO_3$, ZnO, pristine C_3N_4, pristine C_3N_5, and C_3N_5-CN. The effect of PMS dosage on the piezo-photocatalytic system was investigated (Fig. 6f). The removal efficiency of pollutants was not further improved when the PMS dosage was increased to 300 mg/L, which can be attributed to the self-quenching effect of excess PMS [75]. To explore the photocatalytic enhancement with the assistance of ultrasound, the PMS activation via the piezoelectric and photocatalytic systems was investigated separately. As shown in Fig. 6g and Fig. S18, the kinetic constants of degradation in the piezo-photocatalytic system was 7.9 times higher than that of the piezoelectric system and 6.1 times higher than that of the photocatalytic system, indicating the synergistic effect of piezoelectricity and photoelectricity. In the absence of C_3N_{5-x}-CN, the PMS system can remove only about 16.8% of pollutant, proving the critical role of C_3N_{5-x}-CN. Fig. S19 describes the effect of pH on the piezo-photocatalytic activation of PMS. In contrast to the alkaline conditions, acidic conditions are more favorable for the removal of pollutants, which should be attributed to the increased production of radicals by PMS in acidic conditions [76,77]. The degradation of different pollutants verified the universality of the piezo-photocatalytic PMS activation system (Fig. 6h and Fig. S20). With the activation of piezo-photocatalyst, the degradation performance of PMS was substantially improved and the degradation kinetic constants of RhB, MB, TC, and CIP were increased to 2.17, 1.55, 1.44, and 1.35 times, respectively. In the absence of O_2 (Fig. S21), the performance of C_3N_{5-x}-CN piezo-photocatalytic activation of PMS was reduced by only about 15%, indicating that O_2 has a limited effect on PMS activation. Different from piezo-photocatalytic activation of PMS, O_2 is important in piezo-photocatalytic degradation system (Fig. S12). Moreover, the total organic carbon (TOC) removal rate increased from 30.2% to 61.7 after the addition of PMS, proving that the piezo-photocatalytic activation of PMS is more suitable for the mineralization of pollutants (Fig. 6i).

3.3. Characterization of reactive species in piezo-photocatalytic degradation and PMS activation

To further understand the ultrasound-assisted piezo-photocatalytic phenomenon, we performed quenching experiments on the piezocatalytic degradation, photocatalytic degradation and piezo-photocatalytic degradation system, respectively (Fig. 7a and Fig. S22). EDTA-2Na,
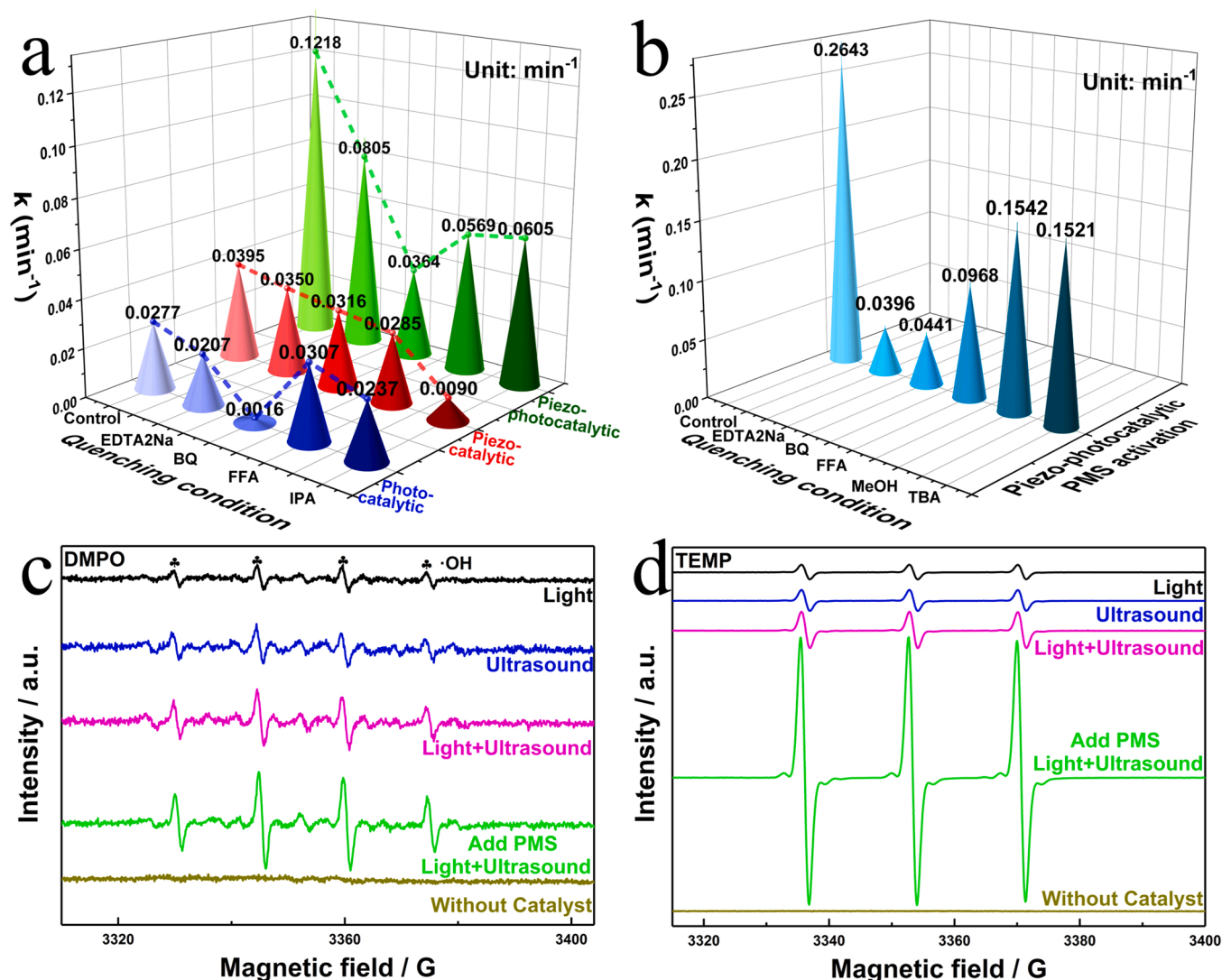

Fig. 7. (a, b) Quenching experiments of different system. ESR data with different trapping agents (c) DMPO, (d) TEMP.

BQ, FFA, and IPA were used as h^+, O_2^-, $^1O_2$, and ·OH quenching agents, respectively. Methanol and tert-butyl alcohol (TBA) were used respectively as·OH/SO_4^- and·OH quenching agents [62]. IPA displayed the strongest inhibitory role in the piezocatalytic degradation system, suggesting that·OH is the main active species. In contrast, photocatalytic and piezo-photocatalytic degradation systems were severely inhibited in the presence of BQ, showing that O_2^- is the main active species in both degradation systems. The piezo-photocatalytic degradation system has significantly higher degradation performance than the photocatalytic degradation system, but their quenching trends are very similar, suggesting that the photocatalytic performance is enhanced with the assistance of ultrasound without changing the main reaction pathway. When 5,5-dimethyl-1-pyrroline-N-oxide (DMPO) and 2,2,6,6-tetramethyl-4-piperidinol (TEMP) were used as trapping agents, as shown in Fig. 7c and 7d, significantly enhanced·OH and $^1O_2$ signals were detected in the piezo-photocatalytic degradation system compared to the photocatalytic degradation or piezocatalytic degradation systems. Nitro

blue tetrazolium (NBT) trapping experiments were conducted to further verify the presence of O_2^-[78]. NBT can react with O_2^- to form monoformazan, thus the O_2^- production could be determined by the decrease of NBT absorbance in UV spectra. As seen in Fig. S23, the C_3N_{5-x}-CN piezo-photocatalytic system has the largest O_2^- yield compared with that obtained from other catalysts. The quenching experiments of the piezo-photocatalytic activation of PMS are summarized in Fig. 7b and Fig. S24. Obviously h^+ and O_2^- are the main active species, which is clearly different from that in the absence of PMS. Furthermore, the addition of PMS also significantly increased the amount of·OH and $^1O_2$ productions, which was evidenced by the DMPO and TEMP trapping experiments. TBA showed a slightly larger inhibitory influence on pollutant degradation than methanol, presumably due to its stronger hydrophobic interaction with catalyst [62]. Based on these experiment results, it is reasonable to conclude that (1) The main ROS of both piezo-photocatalytic and photocatalytic degradation system is O_2^-; (2) Both h^+ and O_2^- are important active species in piezo-photocatalytic
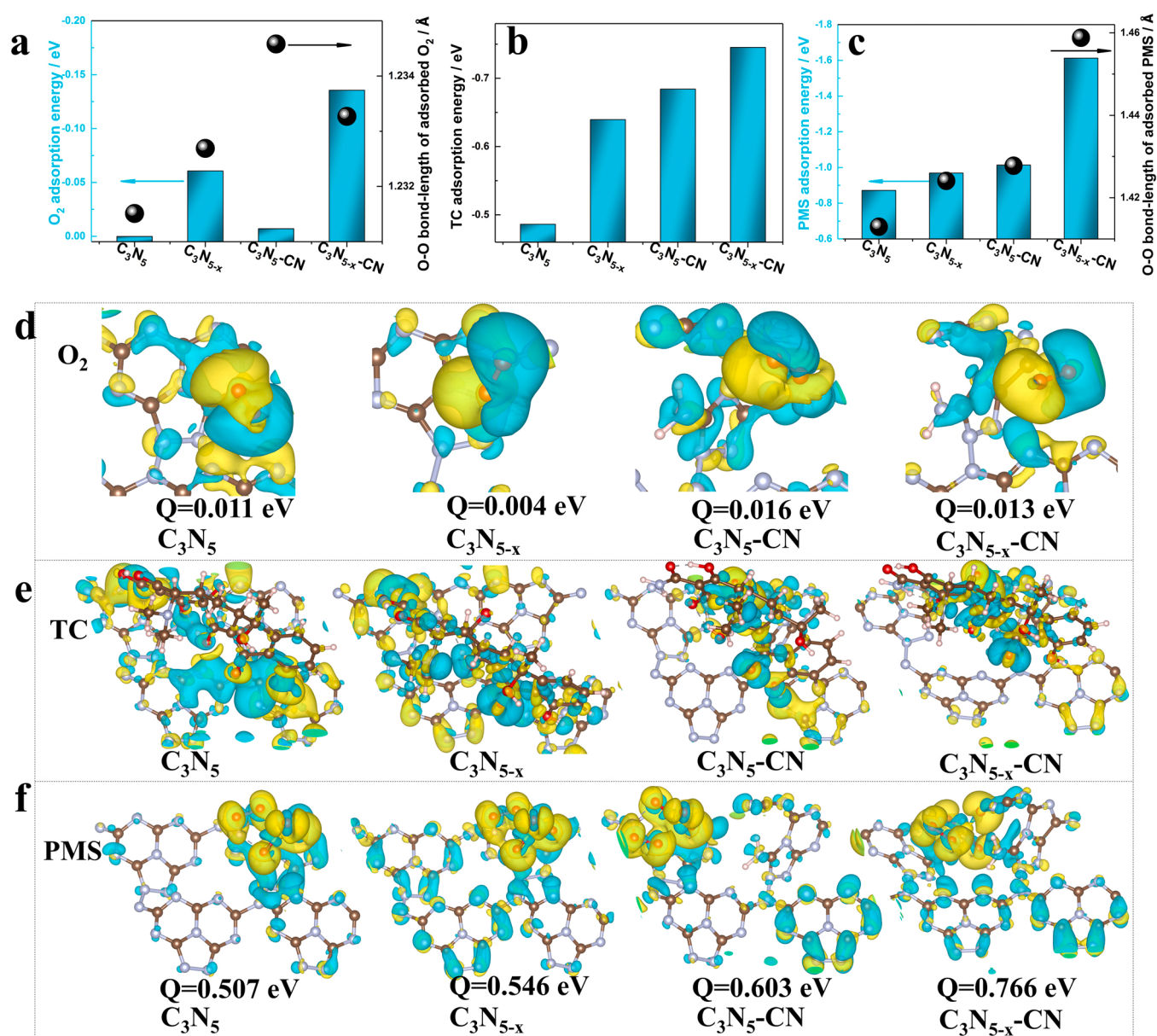
Fig. 8. (a) O_2, (b) TC, and (c) PMS adsorption energy on different C_3N_5-based catalysts. (d) Charge density difference and badercharge data of O_2/catalysts. (e) Charge density difference of TC/catalysts. (f) Charge density difference and badercharge data of PMS/catalysts. Blue and yellow represent electron dissipation and accumulation, respectively.

activation of PMS; (3) Addition of PMS to piezo-photocatalytic degradation system can improve the yield of·OH and $^1O_2$; (4) The piezo-photocatalytic activation of PMS achieves a higher performance than other degradation system.

3.4. Theoretical studies on the synergistic effect of dual-defects in C_3N_5

Compared to other factors, the piezopotential is a promising activity descriptor for piezoelectric catalysis. Some previous works have focused on the magnitude of the piezopotential [27], while largely ignored the involvement of the carriers in the chemical reaction on the catalyst surface. The adsorption behavior of substrates, electron transfer behavior, and reaction pathways in piezo-photocatalysis are all crucial chemical processes that affect the overall catalytic reaction. To elucidate the detailed chemical processes, DFT calculations were conducted for pristine C_3N_5, C_3N_5 with –CN (C_3N_5-CN), C_3N_5 with N vacancy (C_3N_{5-x}), and dual-defect C_3N_5 (C_3N_{5-x}-CN) and the results are presented in Fig. 8. The adsorption behavior of O_2, TC, and PMS with different models was simulated (Fig. 8a-c). And among all models, C_3N_{5-x}-CN shows the highest O_2 adsorption performance (adsorption energy, −0.136 eV), indicating that the dual-defects act synergistically for O_2 adsorption (Fig. 8a). C_3N_{5-x} (adsorption energy, −0.061 eV) adsorbs oxygen more readily than C_3N_5-CN (adsorption energy, −0.007 eV), suggesting that the presence of N vacancies favors O_2 adsorption. The relatively large O-O bond length of O_2 after adsorption on the C_3N_{5-x}-CN surface implies that the dual-defect sites could facilitate the activation of O_2 [5]. Fig. 8b and 8c show a similar adsorption behavior for substrate TC or PMS, indicating that the dual-defect engineering has further increased the adsorption capability of catalyst. In the adsorption model of C_3N_{5-x}-CN, PMS has the longest O-O bond length, implying that the dual-defect engineering could also facilitate the conversion of PMS to radicals [79]. The charge difference density data can be used to reveal the charge redistribution after the adsorption of O_2, TC, or PMS on catalyst. Compared to the adsorption models of pristine C_3N_5, the charge redistribution is more pronounced for C_3N_{5-x}-CN due to its stronger interactions with O_2, TC, or PMS (Fig. 8d-f). The badercharge data also confirm a stronger charge transfer between C_3N_{5-x}-CN and O_2 or PMS, indicating that the dual-defect engineering has a synergistic effect to promote electron transfer between the catalyst and substrate or oxidant.

Based on C_3N_{5-x}-CN, a multifunctional piezo-photocatalytic platform was constructed for pollutant degradation, H_2O_2 generation, and PMS activation. The piezo-photocatalytic mechanism is tentatively proposed in Fig. 9. The N vacancy can efficiently adsorb/activate O_2 to produce various ROS to degrade pollutants (path 1: piezo-photocatalytic degradation) or generate H_2O_2 (path 2: piezo-photocatalytic generation of H_2O_2). The production of H_2O_2 depends mainly on the reduction of O_2 rather than the oxidation of H_2O. The substitution -CN can act as adsorption/activation site for PMS and adsorption site for TC (pathway 3: piezo-photocatalytic activation of PMS). The dual-defect sites exhibit highly synergistic effects by enhancing TC adsorption, O_2 activation and PMS activation performance. Compared to the photocatalytic system or the piezocatalytic system, the piezo-photocatalytic system possesses higher pollutant removal efficiency, H_2O_2 yield, and PMS activation efficiency, confirming the synergistic effect of piezoelectricity and photoelectricity in the C_3N_{5-x}-CN piezo-photocatalytic system. In conclusion, the dual-defect engineering enhances the piezoelectricity, electron transfer and the surface chemistry process of the carbon nitride nanomaterial, thus provides a new strategy for the development of multifunctional piezo-photocatalysts.

3.5. The stability of C_3N_{5-x}-CN piezo-photocatalytic systems

A stability is a key indicator to evaluate the quality of the catalyst. When real water (tap water or Lihu lake water) instead of pure water was used, the piezo-photocatalytic H_2O_2 production was basically unaffected (Fig. 10a). The piezo-photocatalytic degradation and piezo-photocatalytic activation PMS systems in real water system also exhibited similar performance as that in pure water (Fig. 10b, and 10c). These results indicate that this piezo-photocatalytic system has good stability and potential for practical applications.

The recycling performance of C_3N_{5-x}-CN was also investigated (Fig. 10d), and the yield of H_2O_2 changed from 1359 μmol/g/h to 1231 μmol/g/h after 5 cycles. The cycling stability of the piezo-photocatalytic degradation system and the piezo-photocatalytic activation PMS system were further investigated using TC and RhB as substrates (Fig. 10e, f). After 5 cycles, the performance of piezo-photocatalytic degradation system decayed by less than 3%, and the performance of piezo-photocatalytic activation PMS system decayed by less than 5%. The C_3N_{5-x}-CN piezo-photocatalytic system can operate at high concentrations of RhB or TC. As shown in Fig. S25, simply extending the reaction time without raising the catalyst concentration will result in high removal efficiency. The crystal structure and morphology of C_3N_{5-x}-CN have shown little changes before and after use, proving that the C_3N_{5-x}-CN catalyst has excellent stability during the piezo-photocatalytic process. (Fig. S26).

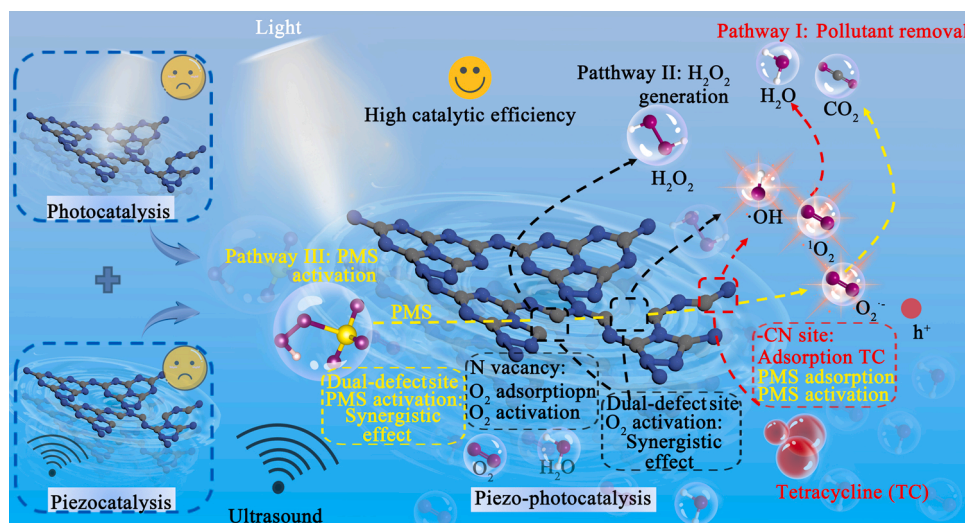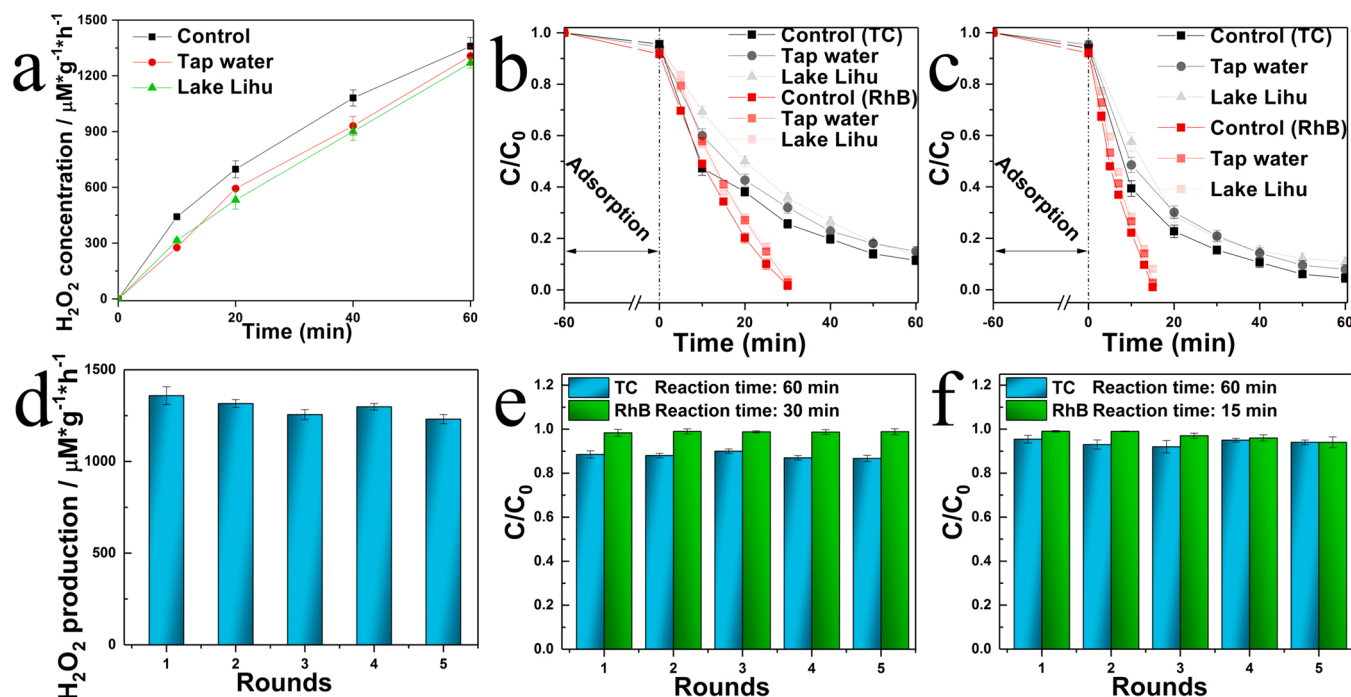**Fig. 9.** Schematic diagram of different C_3N_{5-x}-CN piezo-photocatalytic systems.

Fig. 10. (a) Piezo-photocatalytic H_2O_2 evolution performance, (b) piezo-photocatalytic degradation performance, and (c) piezo-photocatalytic PMS activation performance under different water. Cycling performance of (d) piezo-photocatalytic H_2O_2 evolution system, (e) piezo-photocatalytic degradation system, and (f) piezo-photocatalytic activation of PMS.

4. Conclusions

A laminar structured C_3N_5 with CN and N vacancy (C_3N_{5-x}-CN) was successfully prepared via a simple thermal polymerization/etching method. The superb catalytic performance of C_3N_{5-x}-CN was demonstrated by multifunctional catalytic applications, including pollutant degradation, H_2O_2 production, and PMS activation. Ultrasound assisted enhancement to the photocatalysis of C_3N_{5-x}-CN could be attributed to the piezoelectric effect that promotes the separation of photogenerated carriers. The efficient degradation of RhB and TC was achieved in C_3N_{5-x}-CN piezo-photocatalytic system, and the degradation efficiency can be further enhanced in the presence of PMS. The production of H_2O_2 with a yield of 1359 µmol/g/h was readily achievable in the absence of sacrificial agents. Experimental characterization and computer simulations revealed that the defect structure enhances in-plane polarization, optimizes the electronic structure, facilitates carrier separation/transfer, and exposes more active surface for subsequent redox reactions. Specifically, the N vacancy is the site of O_2 adsorption/activation, and -CN is the site of TC adsorption and PMS adsorption/activation. The dual-defect sites exhibit synergistic effects for efficient substrate adsorption and O_2/PMS activation, leading to enhanced pollutant degradation and H_2O_2 production. The main ROS of both piezo-photocatalytic and photocatalytic degradation system is O_2^-. And both h^+ and O_2^- are important active species in piezo-photocatalytic activation of PMS. The results presented in this study deepen our understanding of the relative activity and synergistic effects of the dual-defect sites and provide a useful guide for the construction and application of high-performance carbon nitride based piezo-photocatalysts.

CRediT authorship contribution statement

Cheng Fu: Investigation, Methodology, Software, Visualization, Data curation, Writing – original draft, Writing – review & editing. **Mengyu Zhao:** Software, Data curation. **Xuan Chen:** Supervision. **Guowei Sun:** Software, Writing – review & editing. **Chan Wang:** Supervision, Funding acquisition. **Qijun Song:** Investigation, Funding

acquisition, Writing – review & editing.

Declaration of Competing Interest

The authors declare that they have no known competing financial interests or personal relationships that could have appeared to influence the work reported in this paper.

Data Availability

Data will be made available on request.

Appendix A. Supporting information

Supplementary data associated with this article can be found in the online version at doi:10.1016/j.apcatb.2023.122752.

References

[1] V. Andrei, G.M. Ucoski, C. Pornrungroj, C. Uswachoke, Q. Wang, D.S. Achilleos, H. Kasap, K.P. Sokol, R.A. Jagt, H. Lu, T. Lawson, A. Wagner, S.D. Pike, D. S. Wright, R.L.Z. Hoye, J.L. MacManus-Driscoll, H.J. Joyce, R.H. Friend, E. Reisner, Floating perovskite-BiVO₄ devices for scalable solar fuel production, Nature 608 (2022) 518–522.
[2] C. Huang, Y. Wen, J. Ma, D. Dong, Y. Shen, S. Liu, H. Ma, Y. Zhang, Unraveling fundamental active units in carbon nitride for photocatalytic oxidation reactions, Nat. Commun. 12 (2021) 320.
[3] C. Chu, Q. Zhu, Z. Pan, S. Gupta, D. Huang, Y. Du, S. Weon, Y. Wu, C. Muhich, E. Stavitski, K. Domen, J.-H. Kim, Spatially separating redox centers on 2D carbon

nitride with cobalt single atom for photocatalytic H₂O₂ production, Proc. Natl. Acad. Sci. 117 (2020) 6376–6382.

[4] Y. Shiraishi, T. Takii, T. Hagi, S. Mori, Y. Kofuji, Y. Kitagawa, S. Tanaka, S. Ichikawa, T. Hirai, Resorcinol–formaldehyde resins as metal-free semiconductor photocatalysts for solar-to-hydrogen peroxide energy conversion, Nat. Mater. 18 (2019) 985–993.

[5] P.M. Xu Zhang, Cong Wang, Liyong Gan, Xianjie Chen, Peng Zhang, Yang Wang, Hui Li, Lihua Wang, Kun Zheng, Unraveling the dual defect sites in graphite carbon nitride for ultra-high photocatalytic H₂O₂ evolution, Energy Environ. Sci. 15 (2022) 830–842.

[6] H. Cheng, H. Lv, J. Cheng, L. Wang, X. Wu, H. Xu, Rational design of covalent heptazine frameworks with spatially separated redox centers for high-efficiency photocatalytic hydrogen peroxide production, Adv. Mater. 34 (2021) 2107480.

[7] L. Pan, S. Sun, Y. Chen, P. Wang, J. Wang, X. Zhang, J.J. Zou, Z.L. Wang, Advances in piezo-phototronic effect enhanced photocatalysis and photoelectrocatalysis, Adv. Eng. Mater. 10 (2020) 2000214.

[8] S. Tu, Y. Guo, Y. Zhang, C. Hu, T. Zhang, T. Ma, H. Huang, Piezocatalysis and piezo-photocatalysis: Catalysts classification and modification strategy, reaction mechanism, and practical application, Adv. Funct. Mater. 30 (2020) 2005158.

[9] Z.L. Wang, Piezopotential gated nanowire devices: piezotronics and piezo-phototronics, Nano Today 5 (2010) 540–552.

[10] J. Yuan, X. Huang, L. Zhang, F. Gao, R. Lei, C. Jiang, W. Feng, P. Liu, Tuning piezoelectric field for optimizing the coupling effect of piezo-photocatalysis, Appl. Catal. B Environ. 278 (2020), 119291.

[11] I.C. Amaechi, A. Hadj Youssef, G. Kolhatkar, D. Rawach, C. Gomez-Yañez, J. P. Claverie, S. Sun, A. Ruediger, Ultrafast microwave-assisted hydrothermal synthesis and photocatalytic behaviour of ferroelectric Fe³⁺-doped BaTiO₃ nanoparticles under simulated sunlight, Catal. Today 360 (2021) 90–98.

[12] S. Lan, C. Yu, F. Sun, Y. Chen, D. Chen, W. Mai, M. Zhu, Tuning piezoelectric driven photocatalysis by La-doped magnetic BiFeO₃-based multiferroics for water purification, Nano Energy 93 (2022), 106792.

[13] T.-M. Chou, S.-W. Chan, Y.-J. Lin, P.-K. Yang, C.-C. Liu, Y.-J. Lin, J.-M. Wu, J.-T. Lee, Z.-H. Lin, A highly efficient Au-MoS₂ nanocatalyst for tunable piezocatalytic and photocatalytic water disinfection, Nano Energy 57 (2019) 14–21.

[14] X. Zhou, S. Wu, C. Li, F. Yan, H. Bai, B. Shen, H. Zeng, J. Zhai, Piezophototronic effect in enhancing charge carrier separation and transfer in ZnO/BaTiO₃ heterostructures for high-efficiency catalytic oxidation, Nano Energy 66 (2019), 104127.

[15] L. Xu, L. Liu, Piezo-photocatalytic fuel cell with atomic Fe@MoS₂ on CFC helical electrode has enhanced peroxymonosulfate activation, pollutant degradation and power generation, Appl. Catal. B, Environ. 304 (2022) 120953.

[16] S.K. In Young Kim+, Xiaoyan Jin, Selvarajan Premkumar, Goutam Chandra, G.P. M. Nam-Suk Lee, Seong-Ju Hwang, Siva Umapathy, Ajayan Vinu*, Ordered mesoporous C3N5 with a combined triazole and triazine framework and its graphene hybrids for the oxygen reduction reaction (ORR), Angew. Chem. Int. Ed. 57 (2018) 17135–17140.

[17] G.P. Mane, S.N. Talapaneni, K.S. Lakhi, H. Ilbeygi, U. Ravon, K. Al-Bahily, T. Mori, D.H. Park, A. Vinu, Highly ordered nitrogen-rich mesoporous carbon nitrides and their superior performance for sensing and photocatalytic hydrogen generation, Angew. Chem. Int. Ed. 56 (2017) 8481–8485.

[18] S. Qi, Y. Fan, J. Wang, X. Song, W. Li, M. Zhao, Metal-free highly efficient photocatalysts for overall water splitting: C3N5 multilayers, Nanoscale 12 (2020) 306–315.

[19] J. Zhang, B. Jing, Z. Tang, Z. Ao, D. Xia, M. Zhu, S. Wang, Experimental and DFT insights into the visible-light driving metal-free C3N5 activated persulfate system for efficient water purification, Appl. Catal. B, Environ. 289 (2021) 120023.

[20] I.Y. Kim, S. Kim, S. Premkumar, J.-H. Yang, S. Umapathy, A. Vinu, Thermodynamically stable mesoporous C3N7 and C3N6 with ordered structure and their excellent performance for oxygen reduction reaction, Small 16 (2020), 1903572.

[21] S.N. Talapaneni, G. Singh, I.Y. Kim, K. AlBahily, Aa.H. Al-Muhtaseb, A.S. Karakoti, E. Tavakkoli, A. Vinu, Nanostructured carbon nitrides for CO₂ capture and conversion, Adv. Mater. 32 (2020), 1904635.

[22] S. Kim, G. Singh, C.I. Sathish, P. Panigrahi, R. Daiyan, X. Lu, Y. Sugi, I.Y. Kim, A. Vinu, Tailoring the pore size, basicity, and binding energy of mesoporous C3N5 for CO₂ capture and conversion, Chem. – Asian J. 16 (2021) 3999–4005.

[23] C. Fu, T. Wu, G. Sun, G. Yin, C. Wang, G. Ran, Q. Song, Dual-defect enhanced piezocatalytic performance of C3N5 for multifunctional applications, Appl. Catal. B, Environ. 323 (2023), 122196.

[24] G. Zhang, Y. Xu, C. He, P. Zhang, H. Mi, Oxygen-doped crystalline carbon nitride with greatly extended visible-light-responsive range for photocatalytic H₂ generation, Appl. Catal. B, Environ. 283 (2021) 119636.

[25] K. Li, W. Cai, Z. Zhang, H. Xie, Q. Zhong, H. Qu, Boron doped C3N5 for photocatalytic nitrogen fixation to ammonia: the key role of boron in nitrogen activation and mechanism, Chem. Eng. J. 435 (2022), 135017.

[26] M.L. Haiyan Wang, Huan Li, Qiujun Lu, Youyu Zhang, Shouzhuo Yao, Porous graphitic carbon nitride with controllable nitrogen vacancies: As promising catalyst for enhanced degradation of pollutant under visible light, Mater. Des. 162 (2019) 210–218.

[27] K. Wang, C. Han, J. Li, J. Qiu, J. Sunarso, S. Liu, The mechanism of piezocatalysis: energy band theory or screening charge effect? Angew. Chem. Int. Ed. 61 (2022), e202110429.

[28] X. Miao, D. Qu, D. Yang, B. Nie, Y. Zhao, H. Fan, Z. Sun, Synthesis of carbon dots with multiple color emission by controlled graphitization and surface functionalization, Adv. Mater. 30 (2018) 1704740.

[29] A. Kumar, P. Raizada, A. Hosseini-Bandegharaei, V.K. Thakur, V.-H. Nguyen, P. Singh, C-, N-vacancy defect engineered polymeric carbon nitride towards photocatalysis: viewpoints and challenges, J. Mater. Chem. A 9 (2021) 111–153.

[30] P. Wang, X. Li, S. Fan, X. Chen, M. Qin, D. Long, M.O. Tadé, S. Liu, Impact of oxygen vacancy occupancy on piezo-catalytic activity of BaTiO₃ nanobelt, Appl. Catal. B, Environ. 279 (2020), 119340.

[31] F.C. Cheng Hu, Yonggang Wang, Na Tian, Tianyi Ma, Yihe Zhang, Hongwei Huang, Exceptional cocatalyst-free photo-enhanced piezocatalytic hydrogen evolution of carbon nitride nanosheets from strong in-plane polarization, Adv. Mater. 33 (2021), 2101751.

[32] R. Tang, D. Gong, Y. Zhou, Y. Deng, C. Feng, S. Xiong, Y. Huang, G. Peng, L. Li, Unique g-C3N4/PDI-g-C3N4 homojunction with synergistic piezo-photocatalytic effect for aquatic contaminant control and H₂O₂ generation under visible light, Appl. Catal. B, Environ. 303 (2022) 120929.

[33] H.Z. Weikang Wang, Shengbo Zhang, Yanyan Liu, Guozhong Wang, Chenghua Sun, Huijun Zhao, Potassium-ion-assisted regeneration of active cyano groups in carbon nitride nanoribbons: visible-light-driven photocatalytic nitrogen reduction, Angew. Chem. Int. Ed. 58 (2019) 16644–16650.

[34] S.S. Sai Zhang, Pengcheng Gu, Ran Ma, Dongli Wei, Guixia Zhao, Tao Wen, Riffat Jehan, Baowei Hu, Xiangke Wang, Visible-light-driven activation of persulfate over cyano and hydroxyl group co-modified mesoporous g-C3N4 for boosting bisphenol A degradation, J. Mater. Chem. A 7 (2019) 5552.

[35] C. Yang, B. Wang, L. Zhang, L. Yin, X. Wang, Synthesis of layered carbonitrides from biotic molecules for photoredox transformations, Angew. Chem. Int. Ed. 56 (2017) 6627–6631.

[36] G. Liu, G. Zhao, W. Zhou, Y. Liu, H. Pang, H. Zhang, D. Hao, X. Meng, P. Li, T. Kako, J. Ye, In situ bond modulation of graphitic carbon nitride to construct p-n homojunctions for enhanced photocatalytic hydrogen production, Adv. Funct. Mater. 26 (2016) 6822–6829.

[37] J. Zhang, M. Zhang, R.Q. Sun, X. Wang, A facile band alignment of polymeric carbon nitride semiconductors to construct isotype heterojunctions, Angew. Chem. Int. Ed. 51 (2012) 10145–10149.

[38] S.P. Dariya Dontsova, Marko Wehle, Zupeng Chen, Christian Fettkenhauer, Guylhaine Clavel, Markus Antonietti, Triazoles: a new class of precursors for the synthesis of negatively charged carbon nitride derivatives, Chem. Mater. 27 (2015) 5170–5179.

[39] Y.W. Youyu Duan, Liyong Gan, Jiazhi Meng, Yajie Feng, Kaiwen Wang, Kai Zhou, Cong Wang, Xiaodong Han, Xiaoyuan Zhou, Amorphous carbon nitride with three coordinate nitrogen (N3C) vacancies for exceptional NOₓ abatement in visible light, Adv. Energy Mater. 11 (2021), 2004001.

[40] W.B. Xiaogang Li, Lei Zhang, Shi Tao, Wangsheng Chu, Qun Zhang, Yi Luo, Changzheng Wu, Yi Xie, Single-Atom Pt as Co-Catalyst for Enhanced Photocatalytic H₂ Evolution, Adv. Mater. 28 (2016) 2427–2431.

[41] G.L. Guigang Zhang, Zhi-An Lan, Lihua Lin, Aleksandr Savateev, Tobias Heil, Spiros Zafeiratos, Xinchen Wang, Markus Antonietti, Optimizing optical absorption, exciton dissociation, and charge transfer of a polymeric carbon nitride with ultrahigh solar hydrogen production activity, Angew. Chem. Int. Ed. 56 (2017) 13445–13449.

[42] Q. Zhang, L. Jiang, J. Wang, Y. Zhu, Y. Pu, W. Dai, Photocatalytic degradation of tetracycline antibiotics using three-dimensional network structure perylene diimide supramolecular organic photocatalyst under visible-light irradiation, Appl. Catal. B Environ. 277 (2020), 119122.

[43] J. Wang, W. Shi, D. Liu, Z. Zhang, Y. Zhu, D. Wang, Supramolecular organic nanofibers with highly efficient and stable visible light photooxidation performance, Appl. Catal. B, Environ. 202 (2017) 289–297.

[44] X. Liu, J. Lu, B.A. Ayele, D. Li, Q. Chen, Coupling of alkaline precipitation and alkali-activated hydrogen peroxide oxidation for reuse of cotton pulp black liquor, J. Clean. Prod. 288 (2021) 125094.

[45] Y. Wei, Y. Zhang, W. Geng, H. Su, M. Long, Efficient bifunctional piezocatalysis of Au/BiVO₄ for simultaneous removal of 4-chlorophenol and Cr(VI) in water, Appl. Catal. B, Environ. 259 (2019) 118084.

[46] Y. Wei, Y. Zhang, J. Miao, W. Geng, M. Long, In-situ utilization of piezo-generated hydrogen peroxide for efficient p-chlorophenol degradation by Fe loading bismuth vanadate, Appl. Surf. Sci. 543 (2021), 148791.

[47] L. Xu, C. Wu, P. Liu, X. Bai, X. Du, P. Jin, L. Yang, X. Jin, X. Shi, Y. Wang, Peroxymonosulfate activation by nitrogen-doped biochar from sawdust for the efficient degradation of organic pollutants, Chem. Eng. J. 387 (2020), 124065.

[48] F. Chen, L.L. Liu, J.J. Chen, W.W. Li, Y.P. Chen, Y.J. Zhang, J.H. Wu, S.C. Mei, Q. Yang, H.Q. Yu, Efficient decontamination of organic pollutants under high salinity conditions by a nonradical peroxymonosulfate activation system, Water Res. 191 (2021), 116799.

[49] H. Kan, H. Soklun, Z. Yang, R. Wu, J. Shen, G. Qu, T. Wang, Purification of dye wastewater using bicarbonate activated hydrogen peroxide: reaction process and mechanisms, Sep. Purif. Technol. 232 (2020), 115974.

[50] S. Zhang, H. Liu, F. Gao, M. Fang, Y. Zhang, Y. Cai, K. Li, M. Kong, X. Tan, The synergetic enhancement of piezo catalytic performance to remove tetracycline by K₂Ti₆O₁₃/TiO₂ composite, J. Alloy. Compd. 900 (2022), 163492.

[51] S. Li, Z. Zhao, D. Yu, J.-Z. Zhao, Y. Su, Y. Liu, Y. Lin, W. Liu, H. Xu, Z. Zhang, Few-layer transition metal dichalcogenides (MoS₂, WS₂, and WSe₂) for water splitting and degradation of organic pollutants: Understanding the piezocatalytic effect, Nano Energy 66 (2019), 104083.

[52] G. Singh, M. Sharma, R. Vaish, Flexible Ag@LiNbO₃/PVDF composite film for piezocatalytic dye/pharmaceutical degradation and bacterial disinfection, ACS Appl. Mater. Inter. 13 (2021) 22914–22925.

[53] Z. Zhuge, X. Liu, T. Chen, Y. Gong, C. Li, L. Niu, S. Xu, X. Xu, Z.A. Alothman, C. Q. Sun, J.G. Shapter, Y. Yamauchi, Highly efficient photocatalytic degradation of

different hazardous contaminants by CaIn$_2$S$_4$-Ti$_3$C$_2$T$_x$ Schottky heterojunction: An experimental and mechanism study, Chem. Eng. J. 421 (2021) 127838.

[54] Z. Wu, Y. Liang, X. Yuan, D. Zou, J. Fang, L. Jiang, J. zhang, H. Yang, Z. Xiao, MXene Ti$_3$C$_2$ derived Z–scheme photocatalyst of graphene layers anchored TiO$_2$/g–C$_3$N$_4$ for visible light photocatalytic degradation of refractory organic pollutants, Chem. Eng. J. 394 (2020), 124921.

[55] Q. Liu, D. Zhai, Z. Xiao, C. Tang, Q. Sun, C.R. Bowen, H. Luo, D. Zhang, Piezo-photoelectronic coupling effect of BaTiO$_3$@TiO$_2$ nanowires for highly concentrated dye degradation, Nano Energy 92 (2022), 106702.

[56] M. Zhu, S. Li, H. Zhang, J. Gao, K.W. Kwok, Y. Jia, L.-B. Kong, W. Zhou, B. Peng, Diffused phase transition boosted dye degradation with Ba (Zr$_x$Ti$_{1−x}$)O$_3$ solid solutions through piezoelectric effect, Nano Energy 89 (2021), 106474.

[57] A. Zhang, Z. Liu, B. Xie, J. Lu, K. Guo, L. Shu, H. Fan, Vibration catalysis of eco-friendly Na$_{0.5}$K$_{0.5}$NbO$_3$-based piezoelectric: An efficient phase boundary catalyst, Appl. Catal. B Environ. 279 (2020), 119353.

[58] L. Chen, Y. Jia, J. Zhao, J. Ma, Z. Wu, G. Yuan, X. Cui, Strong piezocatalysis in barium titanate/carbon hybrid nanocomposites for dye wastewater decomposition, J. Colloid Interface Sci. 586 (2021) 758–765.

[59] Q. Liu, Q. Hu, D. Zhai, Q. Sun, H. Luo, D. Zhang, Superior photo-piezoelectric catalytic performance using Bi$_{0.5}$Na$_{0.5}$TiO$_3$@BiVO$_4$ based cloth, J. Mater. Chem. A 9 (2021) 17841–17854.

[60] J. Xiong, X. Li, J. Huang, X. Gao, Z. Chen, J. Liu, H. Li, B. Kang, W. Yao, Y. Zhu, CN/rGO@BPQDs high-low junctions with stretching spatial charge separation ability for photocatalytic degradation and H$_2$O$_2$ production, Appl. Catal., B, Environ. 266 (2020), 118602.

[61] C. Liu, H. Dai, C. Tan, Q. Pan, F. Hu, X. Peng, Photo-Fenton degradation of tetracycline over Z-scheme Fe-g-C$_3$N$_4$/Bi$_2$WO$_6$ heterojunctions: Mechanism insight, degradation pathways and DFT calculation, Appl. Catal. B, Environ. 310 (2022), 121326.

[62] S. Ye, G. Zeng, X. Tan, H. Wu, J. Liang, B. Song, N. Tang, P. Zhang, Y. Yang, Q. Chen, X. Li, Nitrogen-doped biochar fiber with graphitization from Boehmeria nivea for promoted peroxymonosulfate activation and non-radical degradation pathways with enhancing electron transfer, Appl. Catal. B, Environ. 269 (2020), 118850.

[63] S. Zhang, H. Gao, X. Xu, R. Cao, H. Yang, X. Xu, J. Li, MOF-derived CoN/N-C@SiO$_2$ yolk-shell nanoreactor with dual active sites for highly efficient catalytic advanced oxidation processes, Chem. Eng. J. 381 (2020), 122670.

[64] X. Li, B. Kang, F. Dong, Z. Zhang, X. Luo, L. Han, J. Huang, Z. Feng, Z. Chen, J. Xu, B. Peng, Z.L. Wang, Enhanced photocatalytic degradation and H$_2$/H$_2$O$_2$ production performance of S-pCN/WO$_{2.72}$ S-scheme heterojunction with appropriate surface oxygen vacancies, Nano Energy 81 (2021), 105671.

[65] Y. Kofuji, S. Ohkita, Y. Shiraishi, H. Sakamoto, S. Tanaka, S. Ichikawa, T. Hirai, Graphitic carbon nitride doped with biphenyl diimide: efficient photocatalyst for hydrogen peroxide production from water and molecular oxygen by sunlight, ACS Catal. 6 (2016) 7021–7029.

[66] K. Wang, D. Shao, L. Zhang, Y. Zhou, H. Wang, W. Wang, Efficient piezo-catalytic hydrogen peroxide production from water and oxygen over graphitic carbon nitride, J. Mater. Chem. A 7 (2019) 20383–20389.

[67] L. Zhang, K. Wang, Y. Jia, L. Fang, C. Han, J. Li, Z. Shao, X. Li, J. Qiu, S. Liu, Self-assembled LaFeO$_3$/ZnFe$_2$O$_4$/La$_2$O$_3$ ultracompact hybrids with enhanced piezo-phototronic effect for oxygen activation in ambient conditions, Adv. Funct. Mater. 32 (2022), 2205121.

[68] C. Hu, H. Huang, F. Chen, Y. Zhang, H. Yu, T. Ma, Coupling piezocatalysis and photocatalysis in Bi$_4$NbO$_8$X (X = Cl, Br) polar single crystals, Adv. Funct. Mater. 30 (2020), 1908168.

[69] C. Fu, G. Sun, C. Wang, B. Wei, G. Ran, Q. Song, Fabrication of nitrogen-doped graphene nanosheets anchored with carbon nanotubes for the degradation of tetracycline in saline water, Environ. Res. 206 (2021), 112242.

[70] C. Fu, G. Sun, G. Yin, C. Wang, G. Ran, Q. Song, P/N co-doped carbon sheet for peroxymonosulfate activation: edge sites enhanced adsorption and subsequent electron transfer, Sep. Purif. Technol. 292 (2022), 120922.

[71] J. Wang, S. Wang, Activation of persulfate (PS) and peroxymonosulfate (PMS) and application for the degradation of emerging contaminants, Chem. Eng. J. 334 (2018) 1502–1517.

[72] S. Lan, B. Jing, C. Yu, D. Yan, Z. Li, Z. Ao, M. Zhu, Protrudent iron single-atom accelerated interfacial piezoelectric polarization for self-powered water motion triggered Fenton-like reaction, Small 18 (2022), 2105279.

[73] Y. Chen, S. Lan, M. Zhu, Construction of piezoelectric BaTiO$_3$/MoS$_2$ heterojunction for boosting piezo-activation of peroxymonosulfate, Chin. Chem. Lett. 32 (2021) 2052–2056.

[74] X. Zhang, J. Duan, Y. Tan, Y. Deng, C. Li, Z. Sun, Insight into peroxymonosulfate assisted photocatalysis over Fe$_2$O$_3$ modified TiO$_2$/diatomite composite for highly efficient removal of ciprofloxacin, Sep. Purif. Technol. 293 (2022), 121123.

[75] P. Hu, M. Long, Cobalt-catalyzed sulfate radical-based advanced oxidation: a review on heterogeneous catalysts and applications, Appl. Catal. B, Environ. 181 (2016) 103–117.

[76] W.-D. Oh, Z. Dong, T.-T. Lim, Generation of sulfate radical through heterogeneous catalysis for organic contaminants removal: current development, challenges and prospects, Appl. Catal. B, Environ. 194 (2016) 169–201.

[77] Y. Li, T. Yang, S. Qiu, W. Lin, J. Yan, S. Fan, Q. Zhou, Uniform N-coordinated single-atomic iron sites dispersed in porous carbon framework to activate PMS for efficient BPA degradation via high-valent iron-oxo species, Chem. Eng. J. 389 (2020), 124382.

[78] W.T. Ye Miao, Jun Han, Najun Li, Dongyun Chen, Qingfeng Xu, Jianmei Lu, Oxygen vacancy-induced hydroxyl dipole reorientation in hydroxyapatite for enhanced piezocatalytic activity, Nano Energy 100 (2022), 107473.

[79] X. Duan, J. Kang, W. Tian, H. Zhang, S.-H. Ho, Y.-A. Zhu, Z. Ao, H. Sun, S. Wang, Interfacial-engineered cobalt@carbon hybrids for synergistically boosted evolution of sulfate radicals toward green oxidation, Appl. Catal. B Environ. 256 (2019), 117795.